

Article

One-Step Hydrothermally Synthesized $\text{Ni}_{11}(\text{HPO}_3)_8(\text{OH})_6/\text{Co}_3(\text{HPO}_4)_2(\text{OH})_2$ Heterostructure with Enhanced Rate Performance for Hybrid Supercapacitor Applications

Mingjun Jing ^{1,*}, Kaige Long ¹, Rui Liu ¹, Xingyu Wang ¹, Tianjing Wu ¹, Yirong Zhu ^{2,*}, Lijie Liu ³, Sheng Zhang ⁴ , Yang Zhang ⁵  and Cheng Liu ⁶ 

¹ The College of Chemistry, Xiangtan University, Xiangtan 411105, China

² College of Materials and Advanced Manufacturing, Hunan University of Technology, Zhuzhou 412007, China

³ College of Science, Henan Agricultural University, 63 Agricultural Road, Zhengzhou 450002, China

⁴ Institute of Nanoscience and Engineering, Henan University, Kaifeng 475004, China

⁵ Department of Materials, Henry Royce Institute, University of Manchester, Manchester M13 9PL, UK; yang.zhang-26@postgrad.manchester.ac.uk

⁶ Institut de Ciència de Materials de Barcelona (ICMAB), CSIC, Campus UAB, 08193 Bellaterra, Spain

* Correspondence: jingmingjun@xtu.edu.cn (M.J.); zhuyirong@hut.edu.cn (Y.Z.)

Abstract: Transition metal phosphate is the prospective electrode material for supercapacitors (SCs). It has an open frame construction with spacious cavities and wide aisles, resulting in excellent electric storage capacity. However, the inferior rate behavior and cycling stability of transition metal phosphate materials in alkaline environments pose significant barriers to their application in SCs. Herein, $\text{Ni}_{11}(\text{HPO}_3)_8(\text{OH})_6/\text{Co}_3(\text{HPO}_4)_2(\text{OH})_2$ heterostructured materials synthesized through a one-step hydrothermal process exhibiting remarkable rate capability coupled with exceptional cycling endurance. $\text{Ni}_{11}(\text{HPO}_3)_8(\text{OH})_6/\text{Co}_3(\text{HPO}_4)_2(\text{OH})_2$ samples exhibit a micron-scale structure composed of sheet-like compositions and unique pore structure. The multistage pore structure is favorable for promoting the diffusion of protons and ions, enhancing the sample's electrochemical storage capacity. Upon conducting electrochemical tests, it was observed that $\text{Ni}_{11}(\text{HPO}_3)_8(\text{OH})_6/\text{Co}_3(\text{HPO}_4)_2(\text{OH})_2$ composite electrode surpassed both the standalone $\text{Ni}_{11}(\text{HPO}_3)_8(\text{OH})_6$ and $\text{Co}_3(\text{HPO}_4)_2(\text{OH})_2$ electrode, achieving a remarkable specific capacity of 163 mAh g^{-1} with exceptional stability and efficiency at 1 A g^{-1} . Notably, this electrode also exhibits superior rate performance, maintaining 82.5% and 71% of its original full capacity even at 50 A g^{-1} and 100 A g^{-1} , respectively. Furthermore, it demonstrates superior stability in cycling, retaining a capacity of 92.7% at 10 A g^{-1} after 5000 cycles. Moreover, $\text{Ni}_{11}(\text{HPO}_3)_8(\text{OH})_6/\text{Co}_3(\text{HPO}_4)_2(\text{OH})_2$ and porous carbon (PC) were assembled into a hybrid supercapacitor (HSC). Electrochemical tests reveal an impressive power density of up to 36 kW kg^{-1} and an exceptional energy density of up to 47.4 Wh kg^{-1} for the HSC. Moreover, $\text{Ni}_{11}(\text{HPO}_3)_8(\text{OH})_6/\text{Co}_3(\text{HPO}_4)_2(\text{OH})_2/\text{PC}$ HSC exhibits robust capacity retention stability of 92.9% after enduring 10,000 cycles at 3 A g^{-1} , demonstrating its remarkable durability. This work imparts viewpoints into the design of transition metal phosphate heterostructured materials.



Citation: Jing, M.; Long, K.; Liu, R.; Wang, X.; Wu, T.; Zhu, Y.; Liu, L.; Zhang, S.; Zhang, Y.; Liu, C. One-Step Hydrothermally Synthesized $\text{Ni}_{11}(\text{HPO}_3)_8(\text{OH})_6/\text{Co}_3(\text{HPO}_4)_2(\text{OH})_2$ Heterostructure with Enhanced Rate Performance for Hybrid Supercapacitor Applications. *Batteries* **2024**, *10*, 339. <https://doi.org/10.3390/batteries10100339>

Academic Editor: Leon L. Shaw

Received: 30 August 2024

Revised: 20 September 2024

Accepted: 22 September 2024

Published: 24 September 2024



Copyright: © 2024 by the authors. Licensee MDPI, Basel, Switzerland. This article is an open access article distributed under the terms and conditions of the Creative Commons Attribution (CC BY) license (<https://creativecommons.org/licenses/by/4.0/>).

1. Introduction

As electrochemical energy storage technologies evolve, supercapacitors (SCs) have distinguished themselves among various storage devices because of their environmental friendliness, fast discharging and charging rates, lengthy lifespan, and superior safety features [1–3]. Nevertheless, despite these numerous advantages, there remains a substantial gap between the energy density of SCs and the requirements of commercial applications. Researchers have proposed a feasible approach in the form of a hybrid supercapacitor (HSC) [4,5]. HSC exhibits an exceptional combination of high energy density alongside

robust power density, offering a unique balance in performance [6,7]. The performance of HSC is contingent upon the electrode material utilized. However, conventional cathode materials with a battery type exhibit slow ionic kinetics, while capacitive cathode materials display fast kinetic behavior, rendering it challenging to achieve a suitable match between the two kinetic behaviors [8,9]. In response to the issue, further investigations have revealed that oxides, hydroxides, sulfides, phosphides, and phosphates are all suitable cathode materials for HSC [10–16]. Therefore, developing cathode materials that possess enhanced high kinetics and durability can have a positive effect on overcoming current challenges.

Among various materials, transition metal phosphates have recently attracted much attention, mainly because of their unique properties as both transition metal oxides and transition metal phosphides. This mixture of properties gives them excellent electrochemical performance and high chemical stability [17–19]. Besides, it also has an open structural framework and rich redox behavior, which makes it exhibit excellent energy storage capacity [20,21]. For example, the specific capacitance for $\text{Ni}_3\text{P}_2\text{O}_8$ at 0.5 A g^{-1} is 1464 F g^{-1} [22]. This measured specific capacitance for $\text{Co}_{11}(\text{HPO}_3)_8(\text{OH})_6$ at 0.5 A g^{-1} is 1200 F g^{-1} [23]. Therefore, transition metal phosphates are more attractive when choosing materials for electrodes. Compared with other metal phosphates that have been extensively studied, nickel-based phosphates have a high specific capacitance [24,25]. However, their poor rate behaviors and cyclic stability in alkaline electrolytes limit their large-scale application.

Researchers have implemented various strategies to address the issue, including refining the morphology of materials, constructing a suitable pore structure, designing composite materials and so on [17,26]. For example, an ultra-thin nanosheet-based nickel phosphate lamellar structure attained at 2.0 A g^{-1} current conditions the remarkable specific capacity of 131.6 mAh g^{-1} [27]. $\text{Ni}_3(\text{PO}_4)_2/\text{GF}$ composite nanostructures were prepared, demonstrating a capacitance of 48 mAh g^{-1} at 0.5 A g^{-1} current conditions [28]. While these materials display favorable electrochemical characteristics, there is a continued necessity to identify straightforward and efficacious methodologies for improving nickel-based phosphate rate properties and cycling stability. However, constructing a heterostructure has attracted much attention as a novel approach to creating materials with unique interfaces, elastic structures, and synergistic effects that enhance SCs energy/power density [29–31]. Meanwhile, embedding an internal electric field across the interfaces of heterogeneous structures can potentially expedite ion diffusion, enhancing overall ion transport efficiency [32].

Moreover, the reallocation of charge within the heterostructure components fosters the creation of additional energetic storage sites, enhancing the electrode's reversible capacity and optimizing its energy storage performance [33]. Hence, rationally designed combinations of two materials in heterostructures may yield unprecedented performance due to the complementary effects of different materials. Although previous studies have achieved enhanced electrochemical performance by constructing heterostructures with different components, the synthesis process is complicated. For instance, the amorphous/crystalline nickel manganese phosphate octahydrate heterostructured samples were obtained solely through a hydrothermal process with subsequent annealing in argon gas, demonstrating a specific capacitance of 2351.6 F g^{-1} at 1 A g^{-1} [34]. This specific capacity for $\text{Fe}_{0.4}\text{Co}_{0.6}\text{Se}_2@\text{NiCo-P}$ heterostructured materials was prepared using the two-step electrodeposition method at 1 A g^{-1} with a current condition of 202.3 mAh g^{-1} [35]. Reports on the simple and rapid synthesis of nickel-based metallic phosphate heterostructured materials are scarce. Therefore, it is worthwhile to explore a simple approach to construct a heterostructure of transition metal phosphates.

Herein, the $\text{Ni}_{11}(\text{HPO}_3)_8(\text{OH})_6/\text{Co}_3(\text{HPO}_4)_2(\text{OH})_2$ heterojunction composites were synthesized through a straightforward one-step hydrothermal process, utilizing red phosphorus (RP) as the phosphorous source. This heterostructure effectively has optimized its electronic structure. The redistribution of charges in the heterostructure will induce a greater number of active sites to participate in energy storage, improving the capac-

ity performance of the electrodes. A further examination and analysis of the composition, properties, and structure of the materials is carried out through a series of physical characterization and electrochemical tests. Electrochemical assessments indicate that the $\text{Ni}_{11}(\text{HPO}_3)_8(\text{OH})_6/\text{Co}_3(\text{HPO}_4)_2(\text{OH})_2$ composite electrode boasts enhanced specific capacitance, exceptional rate performance (the capacity retention attains 82.5% and 71%, respectively, when operated at 50 A g^{-1} and 100 A g^{-1} current densities), and impressive recycling capacity. Furthermore, the HSC configured with $\text{Ni}_{11}(\text{HPO}_3)_8(\text{OH})_6/\text{Co}_3(\text{HPO}_4)_2(\text{OH})_2$ and porous carbon (PC) demonstrates outstanding energy/power density and robust cycling endurance. The work gives a practical and effective generalized approach for the preparation of metal-phosphate heterostructured materials.

2. Experimental Section

2.1. Chemicals and Materials

Red phosphorus (RP, AR), nickel nitrate hexahydrate ($\text{Ni}(\text{NO}_3)_2 \cdot 6\text{H}_2\text{O}$, AR), potassium hydroxide (KOH, AR), cobalt nitrate hexahydrate ($\text{Co}(\text{NO}_3)_2 \cdot 6\text{H}_2\text{O}$, AR), ammonia ($\text{NH}_3 \cdot \text{H}_2\text{O}$, AR), and anhydrous ethanol ($\text{C}_2\text{H}_5\text{OH}$, AR) were sourced from Sinopharm Chemical Reagent Co. Ltd. (Shanghai, China). Acetylene black (C, AR) was procured from Shenzhen Kejing Zhida Technology Co., Shenzhen, China; porous carbon (PC, 2 nm) was obtained from Xianfeng Nanomaterials Technology Co., Ltd., Nanjing, China; polytetrafluoroethylene (PTFE, 60%) was acquired from Daikin, Japan; N-methylpyrrolidone (NMP, battery grade) was purchased from Shenzhen Kejing Zhi Technology Co., Ltd., Shenzhen, China. And Nickel foam was obtained from Changde Liyuan New Material Co., Changde, China.

2.2. Synthesis of $\text{Ni}_{11}(\text{HPO}_3)_8(\text{OH})_6$ Cathode Material

After dissolving 0.67 mmol of $\text{Ni}(\text{NO}_3)_2 \cdot 6\text{H}_2\text{O}$ into 50 mL distilled water, 103.75 mg of RP was added and magnetically mixed at 30 min for the solution of deep red color. Then, $\text{NH}_3 \cdot \text{H}_2\text{O}$ was dropped into this solution with the pH adjusted to 8–9. The final solution was moved to the hydrothermal kettle heated to 180 °C and held for 12 h. This reacted solution was naturally cooled to ambient temperature, and the resulting precipitated samples were fully centrifuged alternately into distilled water and subsequently into ethanol to separate any unreacted residue and dried at the temperature of 50 °C, lasting for a period of 12 h to obtain the $\text{Ni}_{11}(\text{HPO}_3)_8(\text{OH})_6$ product.

2.3. Synthesis of $\text{Ni}_{11}(\text{HPO}_3)_8(\text{OH})_6/\text{Co}_3(\text{HPO}_4)_2(\text{OH})_2$ Heterojunction Composites

After dissolving 0.67 mmol $\text{Ni}(\text{NO}_3)_2 \cdot 6\text{H}_2\text{O}$ and 0.67 mmol $\text{Co}(\text{NO}_3)_2 \cdot 6\text{H}_2\text{O}$ into 50 mL of distilled water, 103.75 mg of RP was added and magnetically mixed at 30 min for the solution of deep red color. Then, $\text{NH}_3 \cdot \text{H}_2\text{O}$ was dropped into this solution with pH adjusted to 8–9. The final solution was moved to the hydrothermal kettle heated to 180 °C and held for 12 h. This reacted solution was naturally cooled to ambient temperature, and resulting precipitated samples were fully centrifuged alternately with distilled water and ethanol to separate any unreacted residue and dried at the temperature of 50 °C, lasting for a period of 12 h to afford the $\text{Ni}_{11}(\text{HPO}_3)_8(\text{OH})_6/\text{Co}_3(\text{HPO}_4)_2(\text{OH})_2$ product.

2.4. Material Characteristics

The physical properties of the studied materials were analyzed using a Rigaku D/max 2550 VB⁺ X-ray diffractometer. The physical and structural properties of materials, such as elemental composition, valence states, etc., were studied in depth using an ESCALab 250 X-ray photoelectron spectrometer with Thermo K-Alpha as a light source. The prepared samples were analyzed in detail for morphology, composition, and microstructure using FESEM with Sigma 500. The morphological characteristics and the intricate microstructural features of the samples were thoroughly investigated using the advanced Titan G2 60–300 TEM. Pore sizing and the surface characteristics of materials were analyzed using a specific surface analyzer of Micrometrics ASAP 2020.

2.5. Electrochemical Tests

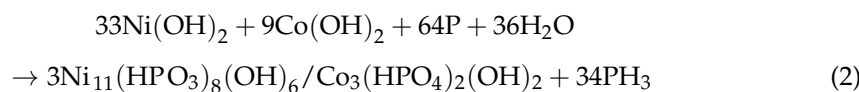
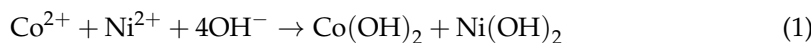
These working electrodes were produced by combining the $\text{Ni}_{11}(\text{HPO}_3)_8(\text{OH})_6/\text{Co}_3(\text{HPO}_4)_2(\text{OH})_2$ sample with acetylene black, serving as a conductive agent, and polytetrafluoroethylene (PTFE), acting as a binder, in a 7:2:1 ratio within an n-methyl-2-pyrrolidinone solution, which served as the dispersant. After mixing, preparation of the paste was uniformly applied to a cleaning nickel foam (collector) and dried in a vacuum oven. Finally, nickel foam was squeezed into working electrodes using a powder press at 10 MPa. The loading of $\text{Ni}_{11}(\text{HPO}_3)_8(\text{OH})_6/\text{Co}_3(\text{HPO}_4)_2(\text{OH})_2$ is $\sim 1 \text{ mg cm}^{-2}$. The CHI 760E electrochemical workstation was used for all electrochemical tests. Therein, the Hg/HgO electrode was used as the reference electrode and the platinum sheet electrode was used as the counter electrode. The cyclic voltammetry (CV) test, alternating current impedance test (EIS), and constant current charge/discharge test (GCD) were used to analyze the electrochemical properties of electrodes. CV curves were acquired over a voltage range of 0~0.6 V, EIS was performed over a frequency range of 100 kHz to 0.01 Hz, and the GCD tests were performed over a potential range of 0~0.55 V.

In addition, HSCs were assembled and used to test their potential for practical applications. The HSC was assembled utilizing $\text{Ni}_{11}(\text{HPO}_3)_8(\text{OH})_6/\text{Co}_3(\text{HPO}_4)_2(\text{OH})_2$ as a cathode, PC as an anode, 2 mol L⁻¹ KOH as an electrolyte, and NKK as the separator in a 2016-type coin cell configuration. To maintain charge equilibrium between the positive and negative components in the HSC, the optimal mass ratio of these two electrodes can be determined using the formula: $m^+/m^- = (C^- \times \Delta V^-)/(C^+ \times \Delta V^+)$, where + and - symbols represent the cathode and anode, respectively, while C and ΔV signify capacity and voltage range, respectively.

3. Results and Discussion

3.1. The Characterizations of Morphology, Composition, and Structure

Figure 1 presents the schematic for the preparation of $\text{Ni}_{11}(\text{HPO}_3)_8(\text{OH})_6$ and $\text{Ni}_{11}(\text{HPO}_3)_8(\text{OH})_6/\text{Co}_3(\text{HPO}_4)_2(\text{OH})_2$ composites using a one-step hydrothermal process. First, $\text{Ni}_{11}(\text{HPO}_3)_8(\text{OH})_6$ material is prepared using red phosphorus as a phosphorus source through the hydrothermal method. To elevate both the specific capacity and cycling stability, the $\text{Ni}_{11}(\text{HPO}_3)_8(\text{OH})_6$ material has been further improved by constructing a heterostructure. Cobalt metal salt, nickel metal salt, RP, and $\text{NH}_3 \cdot \text{H}_2\text{O}$ are thoroughly mixed, and the $\text{Ni}_{11}(\text{HPO}_3)_8(\text{OH})_6/\text{Co}_3(\text{HPO}_4)_2(\text{OH})_2$ product with micrometer structure of flake composition is obtained by a simple hydrothermal method (hydrothermal reaction at 180 °C in a hydrothermal autoclave for 12 h) and centrifugal drying. It is noteworthy that the $\text{Ni}_{11}(\text{HPO}_3)_8(\text{OH})_6/\text{Co}_3(\text{HPO}_4)_2(\text{OH})_2$ composites show a significant change in morphology compared with $\text{Ni}_{11}(\text{HPO}_3)_8(\text{OH})_6$, and their regular lamellar composition structure enhances the energy storage capacity because it enlarges the specific surface area, providing lots of active sites. The $\text{Ni}_{11}(\text{HPO}_3)_8(\text{OH})_6/\text{Co}_3(\text{HPO}_4)_2(\text{OH})_2$ sample is synthesized as follows:



As depicted in Figure 2a, the crystalline nature and structural configuration of the $\text{Ni}_{11}(\text{HPO}_3)_8(\text{OH})_6/\text{Co}_3(\text{HPO}_4)_2(\text{OH})_2$ specimen were characterized using XRD. The XRD diffraction peaks of $\text{Ni}_{11}(\text{HPO}_3)_8(\text{OH})_6/\text{Co}_3(\text{HPO}_4)_2(\text{OH})_2$ sample correspond to the standard cards of $\text{Ni}_{11}(\text{HPO}_3)_8(\text{OH})_6$ (JCPDS No. 81-1065) and $\text{Co}_3(\text{HPO}_4)_2(\text{OH})_2$ (JCPDS No. 80-1996). This suggests that the obtained material is a $\text{Ni}_{11}(\text{HPO}_3)_8(\text{OH})_6/\text{Co}_3(\text{HPO}_4)_2(\text{OH})_2$ heterogeneous structure. The XPS conducted on $\text{Ni}_{11}(\text{HPO}_3)_8(\text{OH})_6/\text{Co}_3(\text{HPO}_4)_2(\text{OH})_2$ sample offered detailed insights into its valence states and surface chemical composition. As illustrated in Figure 2b, the broad XPS spectrum validates the presence of Co, Ni, P,

C, and O, confirming the purity of the specimen without any discernible traces of unintended elements beyond these constituents. Ni 2p spectroscopy with high resolution (Figure 2c) displays two peaks situated at 856.67 eV and 874.52 eV, corresponding to Ni 2p_{3/2} and Ni 2p_{1/2}, respectively. Each of these main signals is accompanied by a satellite peak [36,37]. This matches well with the electronic state of Ni²⁺. Co 2p spectroscopy with high resolution depicted in Figure 2d reveals two distinct peaks at 781.79 eV and 797.83 eV, which are indicative of Co 2p_{3/2} and Co 2p_{1/2} orbitals. This spectral signature confirms the existence of Co²⁺ ions within the system. The high-resolution P 2p spectra (Figure 2e) displays this peak at 133.4 eV attributable to P 2p, indicating the presence of (PO₄)³⁻ on the Ni₁₁(HPO₃)₈(OH)₆/Co₃(HPO₄)₂(OH)₂ surface [38]. The (PO₄)³⁻ form improves the surface activity on Ni₁₁(HPO₃)₈(OH)₆/Co₃(HPO₄)₂(OH)₂. This is consistent with the composition in Ni₁₁(HPO₃)₈(OH)₆/Co₃(HPO₄)₂(OH)₂ according to the above tests.

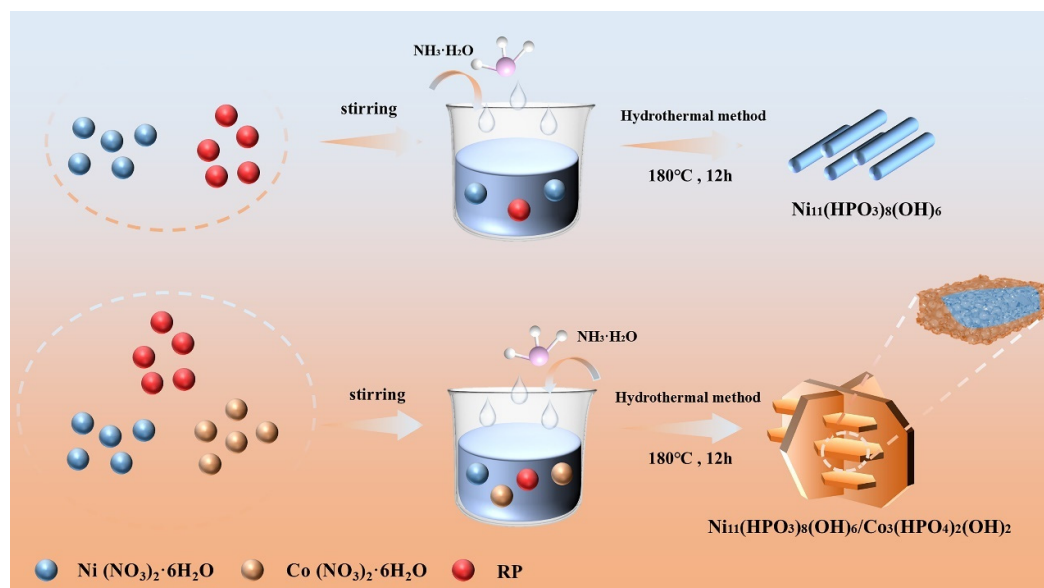


Figure 1. The schematic illustration for hydrothermal preparation of the Ni₁₁(HPO₃)₈(OH)₆ and Ni₁₁(HPO₃)₈(OH)₆/Co₃(HPO₄)₂(OH)₂ samples.

The N₂ adsorption/desorption test of the Ni₁₁(HPO₃)₈(OH)₆/Co₃(HPO₄)₂(OH)₂ heterogeneous structural material is shown in Figure 2f. The Ni₁₁(HPO₃)₈(OH)₆/Co₃(HPO₄)₂(OH)₂ material displays a clear hysteresis ring in the adsorption and desorption isotherms and a type IV isotherm, indicating the existence of their mesoporous structure in Ni₁₁(HPO₃)₈(OH)₆/Co₃(HPO₄)₂(OH)₂. At higher pressures (P/P₀ > 0.9), N₂ adsorption increased rapidly, indicating the existence of microporous structures. The specific surface area of BET for the Ni₁₁(HPO₃)₈(OH)₆/Co₃(HPO₄)₂(OH)₂ material is measured to be 43.2 m² g⁻¹. For the Ni₁₁(HPO₃)₈(OH)₆/Co₃(HPO₄)₂(OH)₂ samples, the pore structure is analyzed by BJH. The Ni₁₁(HPO₃)₈(OH)₆/Co₃(HPO₄)₂(OH)₂ sample exhibits a distinctive hierarchical pore structure, further illuminated by its pore size distribution. This primarily comprises 4 nm mesopores, accompanied by a minimal presence of macropores. The Ni₁₁(HPO₃)₈(OH)₆/Co₃(HPO₄)₂(OH)₂ material's unique pore structure, featuring a dominance of mesopores and a small fraction of macropores, could boost electrochemical energy storage efficiency by facilitating proton and ion diffusion.

Morphology and microstructure are observed for Ni₁₁(HPO₃)₈(OH)₆ and Ni₁₁(HPO₃)₈(OH)₆/Co₃(HPO₄)₂(OH)₂ samples using FESEM. As depicted in Figure 3a-d, the findings demonstrate that the synthesized samples all display a uniform and regular morphology. The Ni₁₁(HPO₃)₈(OH)₆ sample displays a rod shape with a diameter of around 300 nm. In contrast, the Ni₁₁(HPO₃)₈(OH)₆/Co₃(HPO₄)₂(OH)₂ samples exhibit notable alterations. In particular, the Ni₁₁(HPO₃)₈(OH)₆/Co₃(HPO₄)₂(OH)₂ samples display a micrometer-scale structure comprising flake-like units with an overall size of approxi-

mately 9 μm . The EDS and elemental distribution of $\text{Ni}_{11}(\text{HPO}_3)_8(\text{OH})_6$ are signaled in Figure 3e,f. EDS pattern (Figure 3g) reveals that the $\text{Ni}_{11}(\text{HPO}_3)_8(\text{OH})_6/\text{Co}_3(\text{HPO}_4)_2(\text{OH})_2$ material is consisted of Ni, Co, and P. In the atomic ratio of Ni, Co, and P, the approximate ratio is 3:11:10. Figure 3h provides further evidence that the elements Ni, Co and P have a single-form distribution over the structure. According to the above data, the prepared $\text{Ni}_{11}(\text{HPO}_3)_8(\text{OH})_6/\text{Co}_3(\text{HPO}_4)_2(\text{OH})_2$ material has the outstanding advantages of micrometer structure with lamellar composition, high specific surface area and abundant number of mesopores/macropores. Its rich active sites and unique hierarchical pore structure offer the possibility to realize electrochemical properties for the $\text{Ni}_{11}(\text{HPO}_3)_8(\text{OH})_6/\text{Co}_3(\text{HPO}_4)_2(\text{OH})_2$ electrode materials, such as high kinetics and high stability.

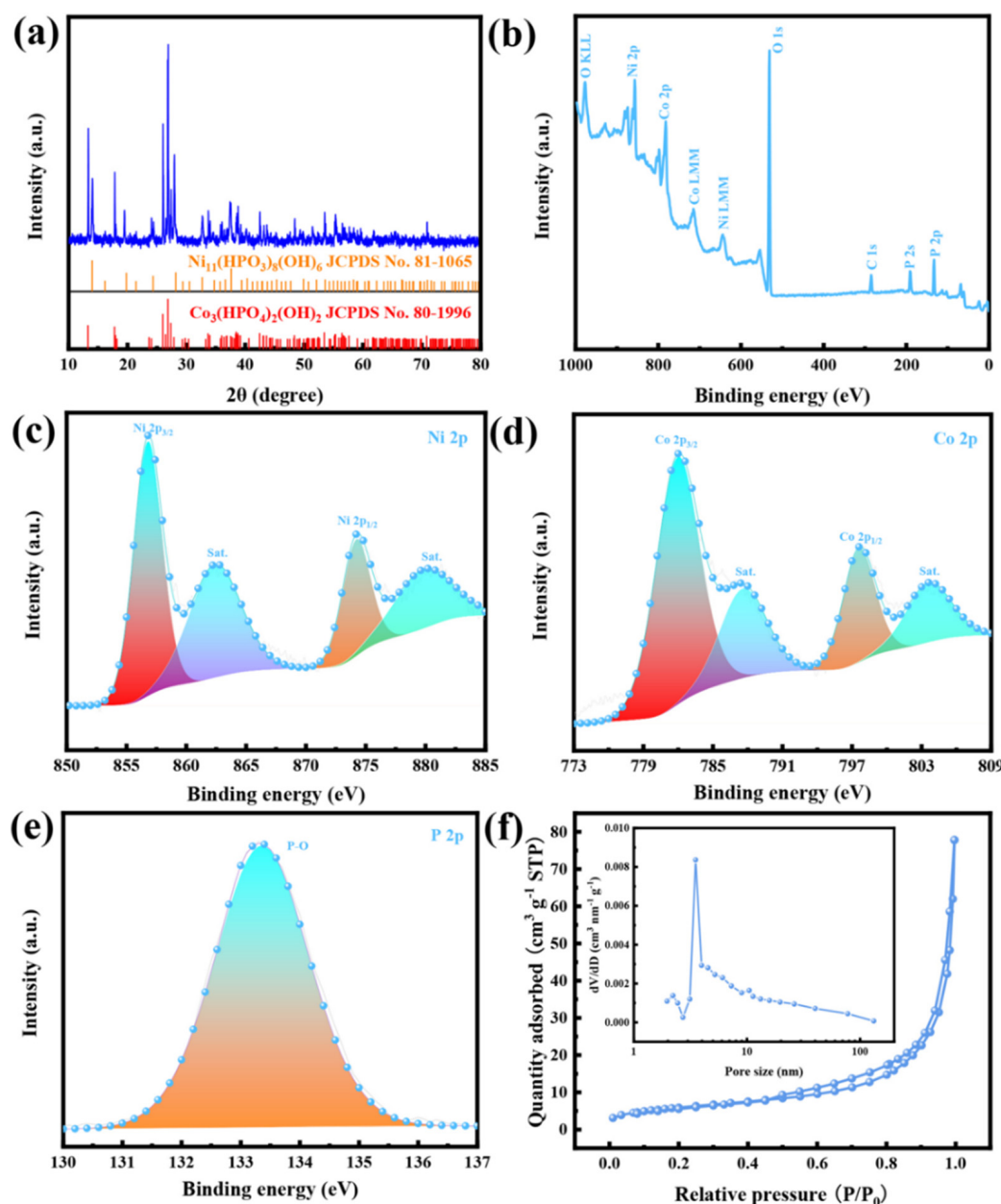


Figure 2. Characterization of $\text{Ni}_{11}(\text{HPO}_3)_8(\text{OH})_6/\text{Co}_3(\text{HPO}_4)_2(\text{OH})_2$ samples: (a) XRD plots; (b–e) XPS spectrum; (f) pore distribution (insert) and sorption–desorption isotherms curves of N_2 .

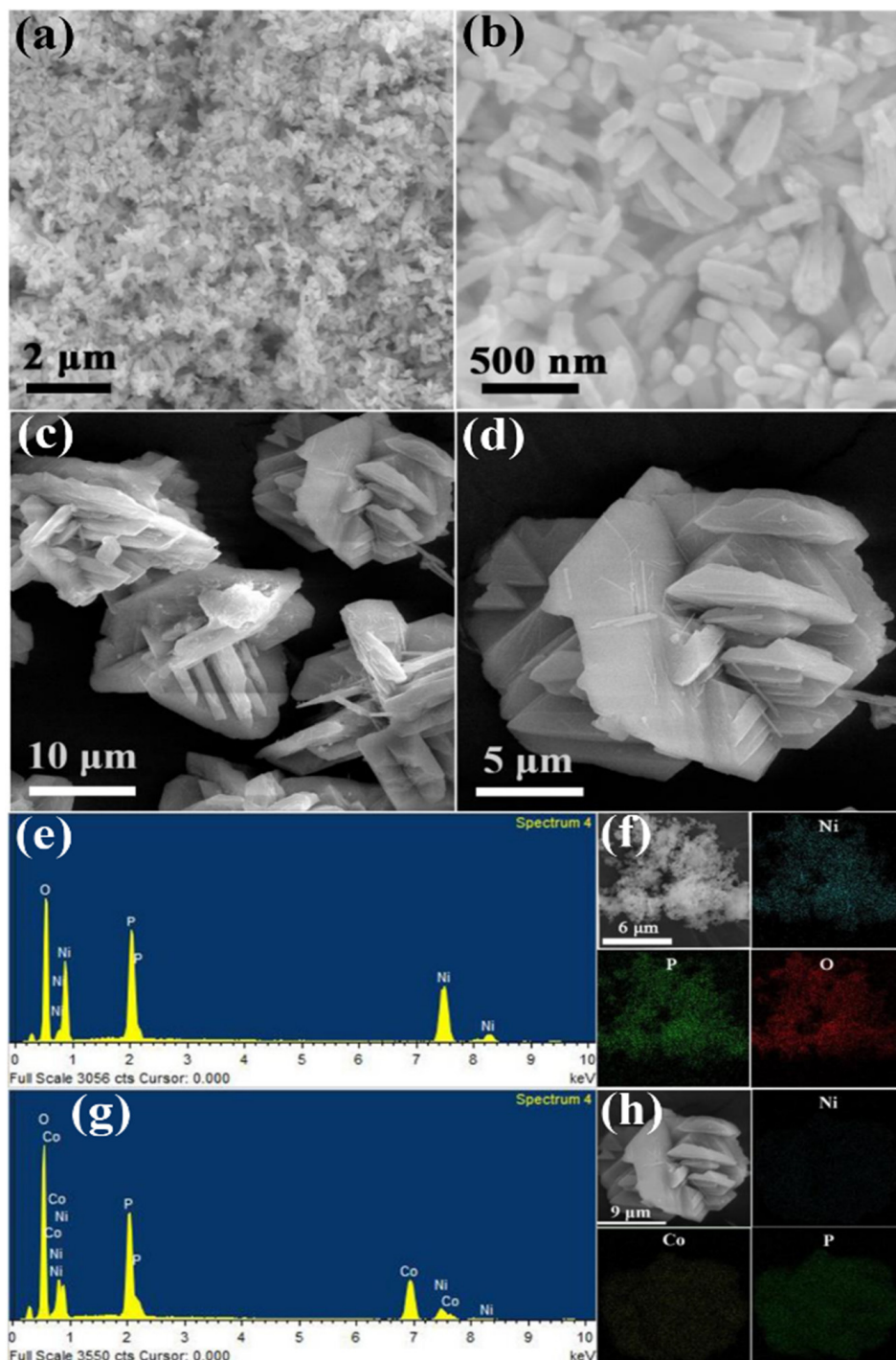
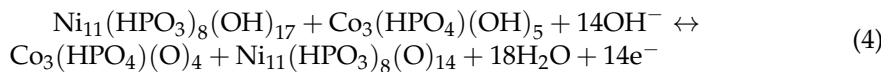
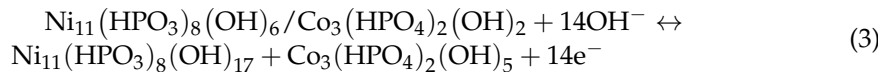


Figure 3. (a,b) FESEM images for $\text{Ni}_{11}(\text{HPO}_3)_8(\text{OH})_6$ at different magnifications. (c,d) FESEM images for $\text{Ni}_{11}(\text{HPO}_3)_8(\text{OH})_6/\text{Co}_3(\text{HPO}_4)_2(\text{OH})_2$ samples with different magnifications. (e,f) EDS and elemental mappings for $\text{Ni}_{11}(\text{HPO}_3)_8(\text{OH})_6$. (g,h) EDS and elemental mappings for the $\text{Ni}_{11}(\text{HPO}_3)_8(\text{OH})_6/\text{Co}_3(\text{HPO}_4)_2(\text{OH})_2$ samples.

3.2. The Electrochemical Performances of Samples

The CV curves for the $\text{Ni}_{11}(\text{HPO}_3)_8(\text{OH})_6$ and $\text{Ni}_{11}(\text{HPO}_3)_8(\text{OH})_6/\text{Co}_3(\text{HPO}_4)_2(\text{OH})_2$ electrodes at 2 mV s^{-1} are presented in Figure 4a. These CV curves display clear redox

peaks, demonstrating typical Faraday characteristics. The equations for the redox reactions could be as follows:



Meanwhile, the $\text{Ni}_{11}(\text{HPO}_3)_8(\text{OH})_6/\text{Co}_3(\text{HPO}_4)_2(\text{OH})_2$ electrode displays a greater area of integration compared to the CV curve for the $\text{Ni}_{11}(\text{HPO}_3)_8(\text{OH})_6$ electrode, indicating the $\text{Ni}_{11}(\text{HPO}_3)_8(\text{OH})_6/\text{Co}_3(\text{HPO}_4)_2(\text{OH})_2$ electrode possesses larger specific capacitance. Comparison is made between two electrodes with GCD curves between 0 and 0.55 V at 1 A g⁻¹ is shown in Figure 4b. Compared to the $\text{Ni}_{11}(\text{HPO}_3)_8(\text{OH})_6$ electrode, the $\text{Ni}_{11}(\text{HPO}_3)_8(\text{OH})_6/\text{Co}_3(\text{HPO}_4)_2(\text{OH})_2$ electrodes demonstrated superior symmetry in their charge-discharge profiles, longer discharge durations, and a broader voltage plateau. These phenomena indicate that the $\text{Ni}_{11}(\text{HPO}_3)_8(\text{OH})_6/\text{Co}_3(\text{HPO}_4)_2(\text{OH})_2$ electrode possesses greater capacity scalability and higher charge conversion efficiency. This specific capacity for the $\text{Ni}_{11}(\text{HPO}_3)_8(\text{OH})_6/\text{Co}_3(\text{HPO}_4)_2(\text{OH})_2$ electrode is determined to be 163.2 mAh g⁻¹, representing a significant increase compared to 79.4 mAh g⁻¹ exhibited by the $\text{Ni}_{11}(\text{HPO}_3)_8(\text{OH})_6$ electrode. The GCD curves (Figure 4c,d) for the $\text{Ni}_{11}(\text{HPO}_3)_8(\text{OH})_6$ and $\text{Ni}_{11}(\text{HPO}_3)_8(\text{OH})_6/\text{Co}_3(\text{HPO}_4)_2(\text{OH})_2$ electrodes show non-linear charge/discharge profiles featuring distinct plateaus, attributable to reversible faraday redox reactions occurring both on the surface and within the electrodes. This further demonstrates their excellent Faraday cell performance. The specific capacities for the $\text{Ni}_{11}(\text{HPO}_3)_8(\text{OH})_6/\text{Co}_3(\text{HPO}_4)_2(\text{OH})_2$ electrodes were 163.2, 161.9, 161.4, 160, 158.3, 150, 134.6, and 115.9 mAh g⁻¹ at 1, 2, 3, 5, 10, 20, 50, and 100 A g⁻¹, respectively, and those of $\text{Ni}_{11}(\text{HPO}_3)_8(\text{OH})_6$ electrode are 79.4, 78.2, 77.6, 76.9, 76.2, 73.3, 65.3 and 54.8 mAh g⁻¹. The capacity retention for the $\text{Ni}_{11}(\text{HPO}_3)_8(\text{OH})_6/\text{Co}_3(\text{HPO}_4)_2(\text{OH})_2$ electrodes is about 71% at 100 A g⁻¹, which exhibits a notably elevated percentage in comparison to 68.9% for $\text{Ni}_{11}(\text{HPO}_3)_8(\text{OH})_6$ electrodes, are exhibited within Figure 4e. The $\text{Ni}_{11}(\text{HPO}_3)_8(\text{OH})_6/\text{Co}_3(\text{HPO}_4)_2(\text{OH})_2$ electrode exhibits high specific capacity at ultra-high current densities, establishing its excellence in practical applications as a high-rate cell-typical electrode material. As shown in Figure 4f, Cyclic stability tests of the $\text{Ni}_{11}(\text{HPO}_3)_8(\text{OH})_6/\text{Co}_3(\text{HPO}_4)_2(\text{OH})_2$ electrodes were conducted through cyclic discharging and charging at 10 A g⁻¹. This capacity retention of the $\text{Ni}_{11}(\text{HPO}_3)_8(\text{OH})_6/\text{Co}_3(\text{HPO}_4)_2(\text{OH})_2$ electrode initially increases to 119% over the first 2000 cycles due to the electrode undergoing a gradual activation process. Subsequently, the capacity retention rate declines to 110.4% and remains stable for approximately 3700 cycles. After 5000 cycles, the $\text{Ni}_{11}(\text{HPO}_3)_8(\text{OH})_6/\text{Co}_3(\text{HPO}_4)_2(\text{OH})_2$ electrode demonstrated remarkable cycling performance, exhibiting an initial capacity retention of 110.4% and a maximum capacity retention of 92.7%. Additionally, the $\text{Ni}_{11}(\text{HPO}_3)_8(\text{OH})_6/\text{Co}_3(\text{HPO}_4)_2(\text{OH})_2$ electrode exhibits a Coulombic efficiency approaching 100%. The $\text{Ni}_{11}(\text{HPO}_3)_8(\text{OH})_6/\text{Co}_3(\text{HPO}_4)_2(\text{OH})_2$ electrode's excellent cycling stabilization may be due to the construction of heterostructures and unique multistage pore structure, along with the -OH groups incorporated within [39].

As illustrated in Table 1, the galvanic properties for the $\text{Ni}_{11}(\text{HPO}_3)_8(\text{OH})_6/\text{Co}_3(\text{HPO}_4)_2(\text{OH})_2$ electrodes are in comparison with other reported metal phosphide and phosphate electrodes. From the results of the comparison, it is found that the $\text{Ni}_{11}(\text{HPO}_3)_8(\text{OH})_6/\text{Co}_3(\text{HPO}_4)_2(\text{OH})_2$ electrode exhibits superior rate performance compared to other already reported electrodes. Furthermore, this method of constructing heterostructures to enhance material properties electrochemically is still rarely reported.

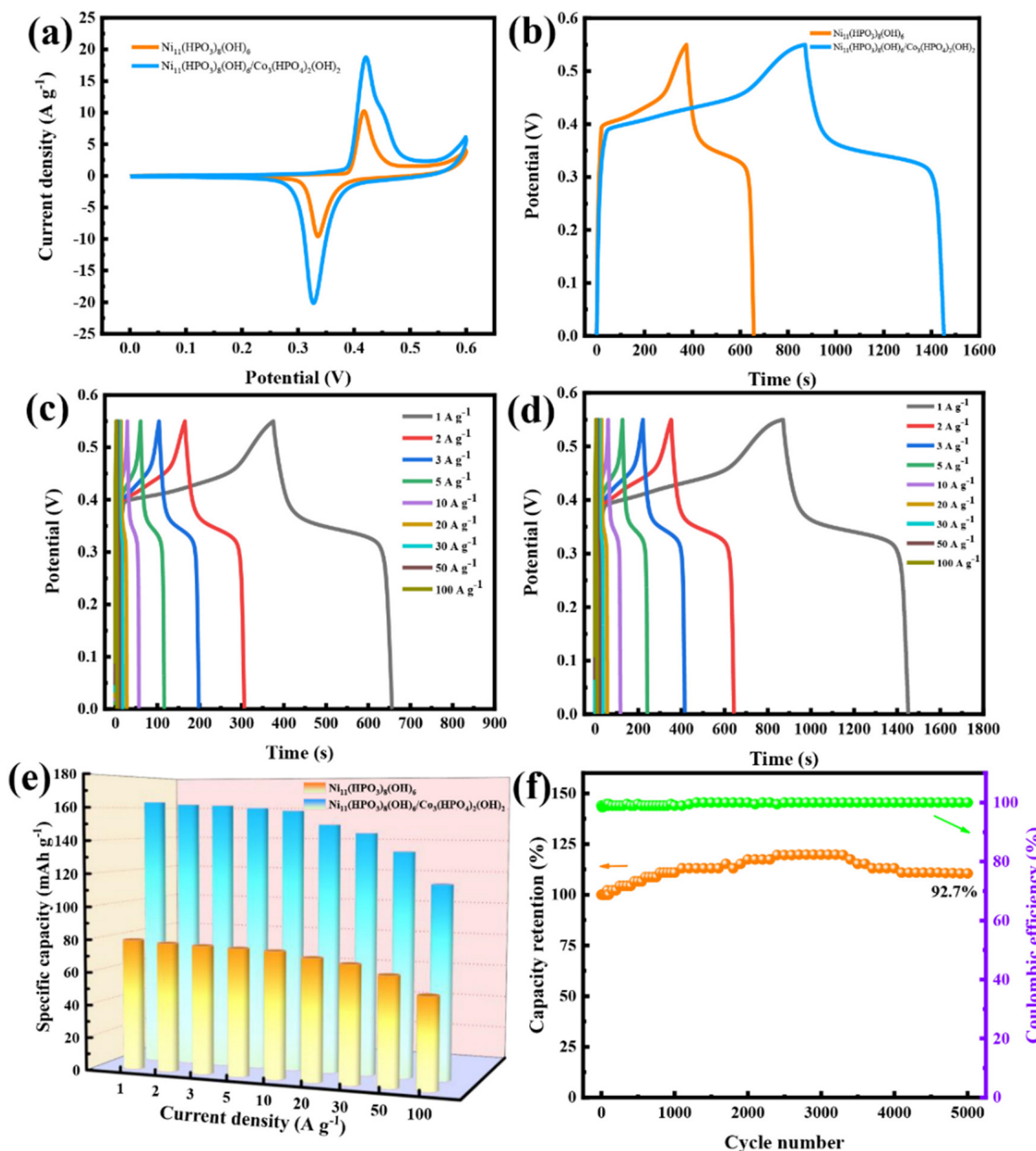


Figure 4. Electrochemical performance of the $\text{Ni}_{11}(\text{HPO}_3)_8(\text{OH})_6$ and $\text{Ni}_{11}(\text{HPO}_3)_8(\text{OH})_6/\text{Co}_3(\text{HPO}_4)_2(\text{OH})_2$ electrodes in the three-electrode system: (a) CV curves at 2 mV s^{-1} , (b) GCD curves at 1 A g^{-1} , (c) GCD curves for the $\text{Ni}_{11}(\text{HPO}_3)_8(\text{OH})_6$ electrode from 1 to 100 A g^{-1} , (d) GCD curves for the $\text{Ni}_{11}(\text{HPO}_3)_8(\text{OH})_6/\text{Co}_3(\text{HPO}_4)_2(\text{OH})_2$ electrode from 1 to 100 A g^{-1} , (e) Rate performance and (f) cyclic stability and Coulombic efficiency for the $\text{Ni}_{11}(\text{HPO}_3)_8(\text{OH})_6/\text{Co}_3(\text{HPO}_4)_2(\text{OH})_2$ electrode.

Figure 5a,b presents display the CV curves for the $\text{Ni}_{11}(\text{HPO}_3)_8(\text{OH})_6$ and $\text{Ni}_{11}(\text{HPO}_3)_8(\text{OH})_6/\text{Co}_3(\text{HPO}_4)_2(\text{OH})_2$ electrodes, respectively, within a range from 5 to 200 mV s^{-1} . The redox peaks are visible on the CV curves, implying classical Faraday cell-type characteristics. Furthermore, the peak current distortion for electrodes is extremely small at 200 mV s^{-1} , displaying that the $\text{Ni}_{11}(\text{HPO}_3)_8(\text{OH})_6/\text{Co}_3(\text{HPO}_4)_2(\text{OH})_2$ electrode possesses rapid charging and discharging characteristics. Figure 5c displays the $I_p-v^{1/2}$ slopes of the oxidation peaks for the $\text{Ni}_{11}(\text{HPO}_3)_8(\text{OH})_6$ and $\text{Ni}_{11}(\text{HPO}_3)_8(\text{OH})_6/\text{Co}_3(\text{HPO}_4)_2(\text{OH})_2$ electrodes, which are 17.8 and 32.1 , respectively. Additionally, the $I_p-v^{1/2}$ slopes of the reduction peaks for these electrodes are -17.3 and -30.6 , respectively. The

two electrodes undergo a semi-quantitative analysis according to the charge storage mechanism to facilitate a deeper understanding of their electrochemical behavior, where this peak current I_p on scanning rate v is shown in the below equation: $I_p = a v^b$, $\log I_p = b \log v + \log a$, where the peak current denoted by the symbol I_p . The scan velocity is represented by v . Meanwhile, a and b serve as constants. Figure 5d displays the $\log I_p$ - $\log v$ fit line. The b -values for electrodes $\text{Ni}_{11}(\text{HPO}_3)_8(\text{OH})_6$ and $\text{Ni}_{11}(\text{HPO}_3)_8(\text{OH})_6/\text{Co}_3(\text{HPO}_4)_2(\text{OH})_2$ are 0.7 and 0.75, respectively. Their values, ranging between 0.5 and 1, suggest a combined influence of diffusion and capacitive-controlled storage mechanisms, with capacitive control predominating. The above conclusions are subject to further verification.

Table 1. A summary of metal phosphides and phosphates used in SCs together with their corresponding electrochemical performance.

Material	Specific Capacity (mAh g ⁻¹)	Rate Retention	Cyclic Property	Ref.
NiCoP/NiCo-OH	152.8 at 1 A g ⁻¹	60% (1–10 A g ⁻¹)	88% after 1000 cycles	[40]
NiCoP	160.8 at 1 A g ⁻¹	81% (1–16 A g ⁻¹)	/	[41]
Porous NiCoP	158.6 at 1 A g ⁻¹	72.8% (1–20 A g ⁻¹)	72% after 3000 cycles	[42]
Ni-Co phosphate	125.8 at 1 A g ⁻¹	63.4% (1–10 A g ⁻¹)	93% after 8000 cycles	[43]
$\text{NH}_4\text{Co}_{0.33}\text{Ni}_{0.67}\text{PO}_4 \cdot \text{H}_2\text{O}$	158 at 1.5 A g ⁻¹	66% (1.5–30 A g ⁻¹)	57% after 1000 cycles	[44]
$\text{Ni}_x\text{Co}_{3-x}(\text{PO}_4)_2$	94.2 at 1 A g ⁻¹	81.4% (1–10 A g ⁻¹)	85% after 1000 cycles	[45]
$\text{Co}_{0.5}\text{Ni}_{0.5}$ pyrophosphate	161 at 1.5 A g ⁻¹	/	/	[46]
Cobalt-doped Ni phosphite	83.6 at 0.5 A g ⁻¹	85% (0.5–5 A g ⁻¹)	93% after 8000 cycles	[47]
$(\text{Ni},\text{Co})_3(\text{PO}_4)_2 \cdot 8\text{H}_2\text{O}/(\text{NH}_4)$ $(\text{Ni},\text{Co})\text{PO}_4 \cdot 0.67\text{H}_2\text{O}$	141 at 0.5 A g ⁻¹	88% (0.5–24 A g ⁻¹)	/	[48]
Ni-Co phosphate	147 at 0.2 A g ⁻¹	85% (0.2–10 A g ⁻¹)	/	[49]
Co(P, S)/CC	101.6 at 1 A g ⁻¹	56% (1–20 A g ⁻¹)	/	[50]
$\text{Ni}_{11}(\text{HPO}_3)_8(\text{OH})_6/\text{Co}_3(\text{HPO}_4)_2(\text{OH})_2$	163.2 at 1 A g ⁻¹	96.9% (1–10 A g ⁻¹) 91.9% (1–20 A g ⁻¹) 71% (1–100 A g ⁻¹)	92.7% after 5000 cycles	This work

Furthermore, the diffusion-controlled/surface capacitive charge contributions can be quantified by the below equations: $I_p(v) = k_1 v + k_2 v^{1/2}$. Here, $k_1 v$ is for surface capacitance, and $k_2 v^{1/2}$ is for diffusion control. Figure 5e,f depicts comparative contributions of capacitive and diffusive processes in the $\text{Ni}_{11}(\text{HPO}_3)_8(\text{OH})_6$ and $\text{Ni}_{11}(\text{HPO}_3)_8(\text{OH})_6/\text{Co}_3(\text{HPO}_4)_2(\text{OH})_2$ electrodes at 10 mV s⁻¹, respectively. This capacitance-controlled contribution for $\text{Ni}_{11}(\text{HPO}_3)_8(\text{OH})_6$ is 72.1%, while that of $\text{Ni}_{11}(\text{HPO}_3)_8(\text{OH})_6/\text{Co}_3(\text{HPO}_4)_2(\text{OH})_2$ is 80.6%. It is reiterated that the capacitive characteristic predominates over the overall capacity of the electrodes. Figure 5g displays capacitive influences from both electrodes at varying scan velocities. These distinct capacitive behaviors of the two electrodes demonstrated an increase as the scanning velocity escalated. Moreover, the capacitive contributions of the $\text{Ni}_{11}(\text{HPO}_3)_8(\text{OH})_6/\text{Co}_3(\text{HPO}_4)_2(\text{OH})_2$ electrode are observed to be greater than those of the $\text{Ni}_{11}(\text{HPO}_3)_8(\text{OH})_6$ electrode at varying scan rates. Consistent with the rate performance trend, the $\text{Ni}_{11}(\text{HPO}_3)_8(\text{OH})_6/\text{Co}_3(\text{HPO}_4)_2(\text{OH})_2$ electrode exhibits a dominant surface capacitance of 74.6% at 2 mV s⁻¹, indicative of its typical cell behavior under low scanning rates. The surface capacitance contribution at 100 mV s⁻¹, at 99.8%, is concordant with CV analysis outcomes. EIS tests were con-

ducted to investigate the electrode kinetics further. Figure 5h showcases Nyquist plots for the $\text{Ni}_{11}(\text{HPO}_3)_8(\text{OH})_6$ and $\text{Ni}_{11}(\text{HPO}_3)_8(\text{OH})_6/\text{Co}_3(\text{HPO}_4)_2(\text{OH})_2$ electrodes. The radius of the semicircular arc signifies the impedance to charge migration (R_{ct}), and the x-intercept represents internal resistance (R_s) in the high-frequency region. Furthermore, the $\text{Ni}_{11}(\text{HPO}_3)_8(\text{OH})_6$ and $\text{Ni}_{11}(\text{HPO}_3)_8(\text{OH})_6/\text{Co}_3(\text{HPO}_4)_2(\text{OH})_2$ electrodes demonstrated a markedly low R_{ct} , indicating the process of charge translocation transpires across the electrode-electrolyte juncture. The line slope of the $\text{Ni}_{11}(\text{HPO}_3)_8(\text{OH})_6/\text{Co}_3(\text{HPO}_4)_2(\text{OH})_2$ electrode is closer to 90° across the lower frequency spectrum, which suggests that the $\text{Ni}_{11}(\text{HPO}_3)_8(\text{OH})_6/\text{Co}_3(\text{HPO}_4)_2(\text{OH})_2$ electrode exhibits greater capacitive properties. Moreover, $\text{Ni}_{11}(\text{HPO}_3)_8(\text{OH})_6/\text{Co}_3(\text{HPO}_4)_2(\text{OH})_2$ exhibits a more pronounced linear gradient than that observed in $\text{Ni}_{11}(\text{HPO}_3)_8(\text{OH})_6$. The electrode's enhanced ion diffusion rate stems from the unique hierarchical porous architecture for $\text{Ni}_{11}(\text{HPO}_3)_8(\text{OH})_6/\text{Co}_3(\text{HPO}_4)_2(\text{OH})_2$, coupled with its superior conductivity. The EIS analysis results serve to further corroborate the assertion that the $\text{Ni}_{11}(\text{HPO}_3)_8(\text{OH})_6/\text{Co}_3(\text{HPO}_4)_2(\text{OH})_2$ electrode exhibits superior internal resistance and commendable reaction kinetics in comparison to the $\text{Ni}_{11}(\text{HPO}_3)_8(\text{OH})_6$ electrode.

For evaluating the potential application for $\text{Ni}_{11}(\text{HPO}_3)_8(\text{OH})_6/\text{Co}_3(\text{HPO}_4)_2(\text{OH})_2$ in energy storage, the HSC was constructed in 2 mol L^{-1} KOH utilizing PC as anode and this material as a cathode. Figure 6a illustrates the total voltage window of the HSC, derived from analyzing the CV profiles for the PC and $\text{Ni}_{11}(\text{HPO}_3)_8(\text{OH})_6/\text{Co}_3(\text{HPO}_4)_2(\text{OH})_2$ electrodes independently at 10 mV s^{-1} in 2 mol L^{-1} KOH electrolytes. The CV curves of the PCs exhibit a rectangular shape and demonstrate excellent electric double layer (EDL) behavior. The potential ranges for the PC and $\text{Ni}_{11}(\text{HPO}_3)_8(\text{OH})_6/\text{Co}_3(\text{HPO}_4)_2(\text{OH})_2$ electrodes are confined to -1 to 0 V as well as 0 to 0.6 V. Figure 6b displays rectangular shape for the CV curves for $\text{Ni}_{11}(\text{HPO}_3)_8(\text{OH})_6/\text{Co}_3(\text{HPO}_4)_2(\text{OH})_2 // \text{PC}$ HSC within $2 \sim 100 \text{ mV s}^{-1}$, with significant redox peak characteristics within the 0~1.5 V. Meanwhile, CV curves exhibited minimal variation across varying scan rates, signifying the device's outstanding rate performance. The capacitance characteristics for the $\text{Ni}_{11}(\text{HPO}_3)_8(\text{OH})_6/\text{Co}_3(\text{HPO}_4)_2(\text{OH})_2 // \text{PC}$ HSC underwent additional examination through performing GCD tests between $2 \sim 100 \text{ A g}^{-1}$. Figure 6c makes known that the symmetric GCD curve of the $\text{Ni}_{11}(\text{HPO}_3)_8(\text{OH})_6/\text{Co}_3(\text{HPO}_4)_2(\text{OH})_2 // \text{PC}$ HSC shows good electrochemical reversibility. Figure 6d reveals that the $\text{Ni}_{11}(\text{HPO}_3)_8(\text{OH})_6/\text{Co}_3(\text{HPO}_4)_2(\text{OH})_2 // \text{PC}$ HSC boasts a specific capacitance value of 151.6 F g^{-1} when tested at 2 A g^{-1} , and retains a capacitance of 58.8 F g^{-1} at 100 A g^{-1} . This underscores the device's high specific capacitance, attributable to the optimal chemical composition, distinctive layered porous architecture, and exceptional electronic conductivity for the $\text{Ni}_{11}(\text{HPO}_3)_8(\text{OH})_6/\text{Co}_3(\text{HPO}_4)_2(\text{OH})_2$ materials. Figure 6e illustrates the Ragone diagram of the $\text{Ni}_{11}(\text{HPO}_3)_8(\text{OH})_6/\text{Co}_3(\text{HPO}_4)_2(\text{OH})_2 // \text{PC}$ HSC. The energy density for $\text{Ni}_{11}(\text{HPO}_3)_8(\text{OH})_6/\text{Co}_3(\text{HPO}_4)_2(\text{OH})_2 // \text{PC}$ HSC reaches 47.4 Wh kg^{-1} at 660 Wh kg^{-1} , and maintains 18.4 Wh kg^{-1} even at a super-high 33 kW kg^{-1} . This surpasses the energy density reported for previous cobalt-based phosphide and nickel-based phosphate HSCs. For example, $\text{Co}_3(\text{PO}_4)_2 // \text{AC}$ ($26.66 \text{ Wh kg}^{-1} / 750 \text{ W kg}^{-1}$) [51], $\text{Co}_3(\text{PO}_4)_2 \cdot 4\text{H}_2\text{O}/\text{GF} // \text{C-FP}$ ($24 \text{ Wh kg}^{-1} / 468 \text{ W kg}^{-1}$) [52], $\text{NH}_4\text{CoPO}_4 \cdot \text{H}_2\text{O} // \text{AC}$ ($10.4 \text{ Wh kg}^{-1} / 141.3 \text{ W kg}^{-1}$) [53], $\text{NiCoP@NF} // \text{AC}$ ($27 \text{ Wh kg}^{-1} / 647 \text{ W kg}^{-1}$) [54], $\text{Ni-Co-P/PO}_x // \text{RGO}$ ($36.84 \text{ Wh kg}^{-1} / 727.8 \text{ W kg}^{-1}$) [55], $\text{NiCoO}_2/\text{NiCoP} // \text{AC}$ ($40.32 \text{ Wh kg}^{-1} / 800.18 \text{ W kg}^{-1}$) [56], $\text{Co}_3(\text{PO}_4)_2 \cdot 8\text{H}_2\text{O} // \text{AC}$ ($29.29 \text{ Wh kg}^{-1} / 468.75 \text{ W kg}^{-1}$) [57]. The cycling properties for $\text{Ni}_{11}(\text{HPO}_3)_8(\text{OH})_6/\text{Co}_3(\text{HPO}_4)_2(\text{OH})_2 // \text{PC}$ HSC were examined through the implementation of cycling tests (Figure 6f). After 10,000 cycles, $\text{Ni}_{11}(\text{HPO}_3)_8(\text{OH})_6/\text{Co}_3(\text{HPO}_4)_2(\text{OH})_2 // \text{PC}$ HSC demonstrated remarkable cycling performance, exhibiting capacity retention of up to 92.9% at 3 A g^{-1} . Their feasibility in practical applications is confirmed by these test data.

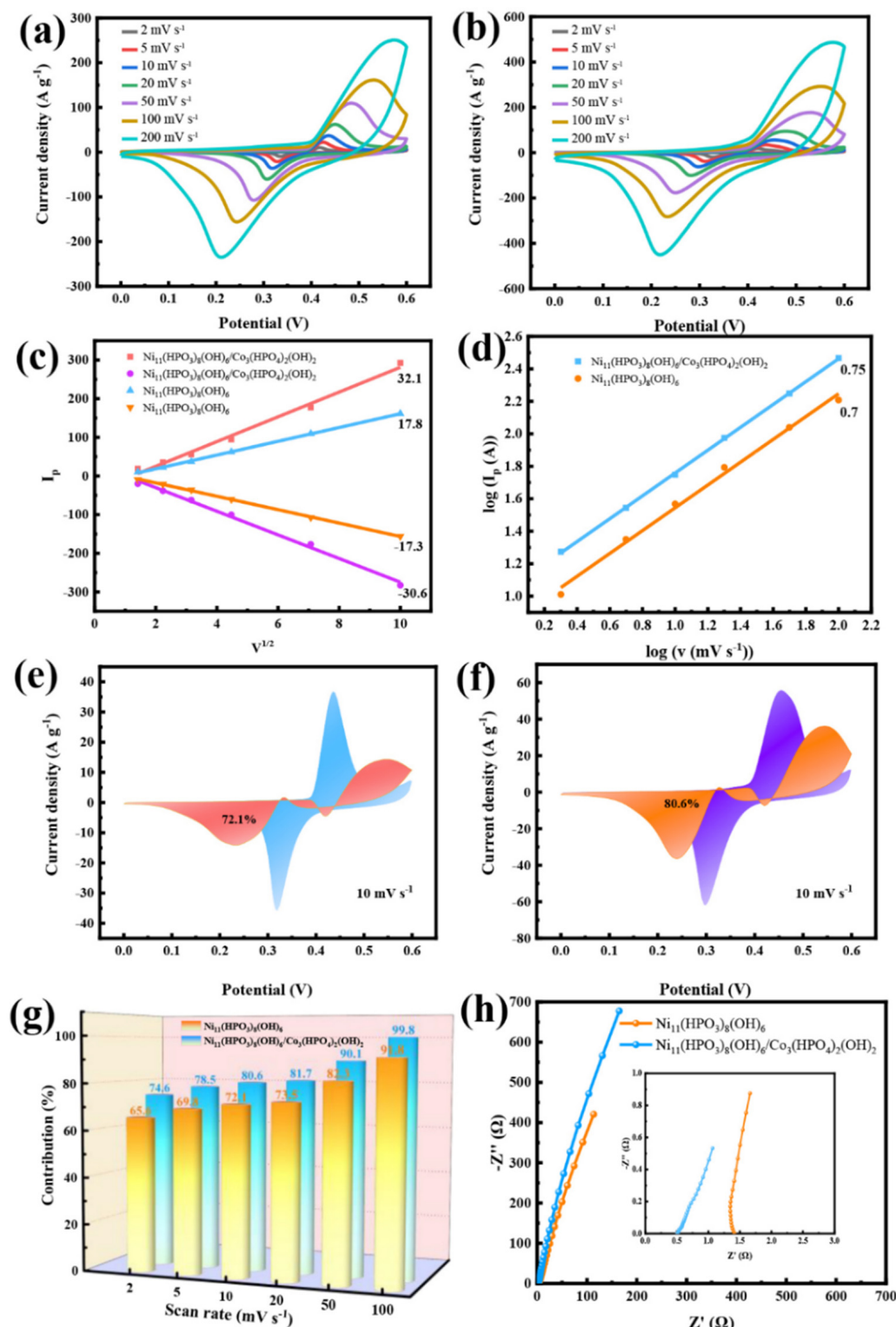


Figure 5. Electrochemical performance of the $\text{Ni}_{11}(\text{HPO}_3)_8(\text{OH})_6$ and $\text{Ni}_{11}(\text{HPO}_3)_8(\text{OH})_6/\text{Co}_3(\text{HPO}_4)_2(\text{OH})_2$ electrodes: **(a)** $\text{Ni}_{11}(\text{HPO}_3)_8(\text{OH})_6$ CV curves between 2 and 200 mV s^{-1} , **(b)** $\text{Ni}_{11}(\text{HPO}_3)_8(\text{OH})_6/\text{Co}_3(\text{HPO}_4)_2(\text{OH})_2$ CV curves between 2 and 200 mV s^{-1} , **(c)** linear relation of $I_p-v^{1/2}$, **(d)** $\log I_p$ - $\log v$ linear relationship, **(e,f)** diffusion and capacitive contributions at 10 mV s^{-1} , **(g)** capacitive contribution comparison from 2 to 100 mV s^{-1} , and **(h)** the EIS plots.

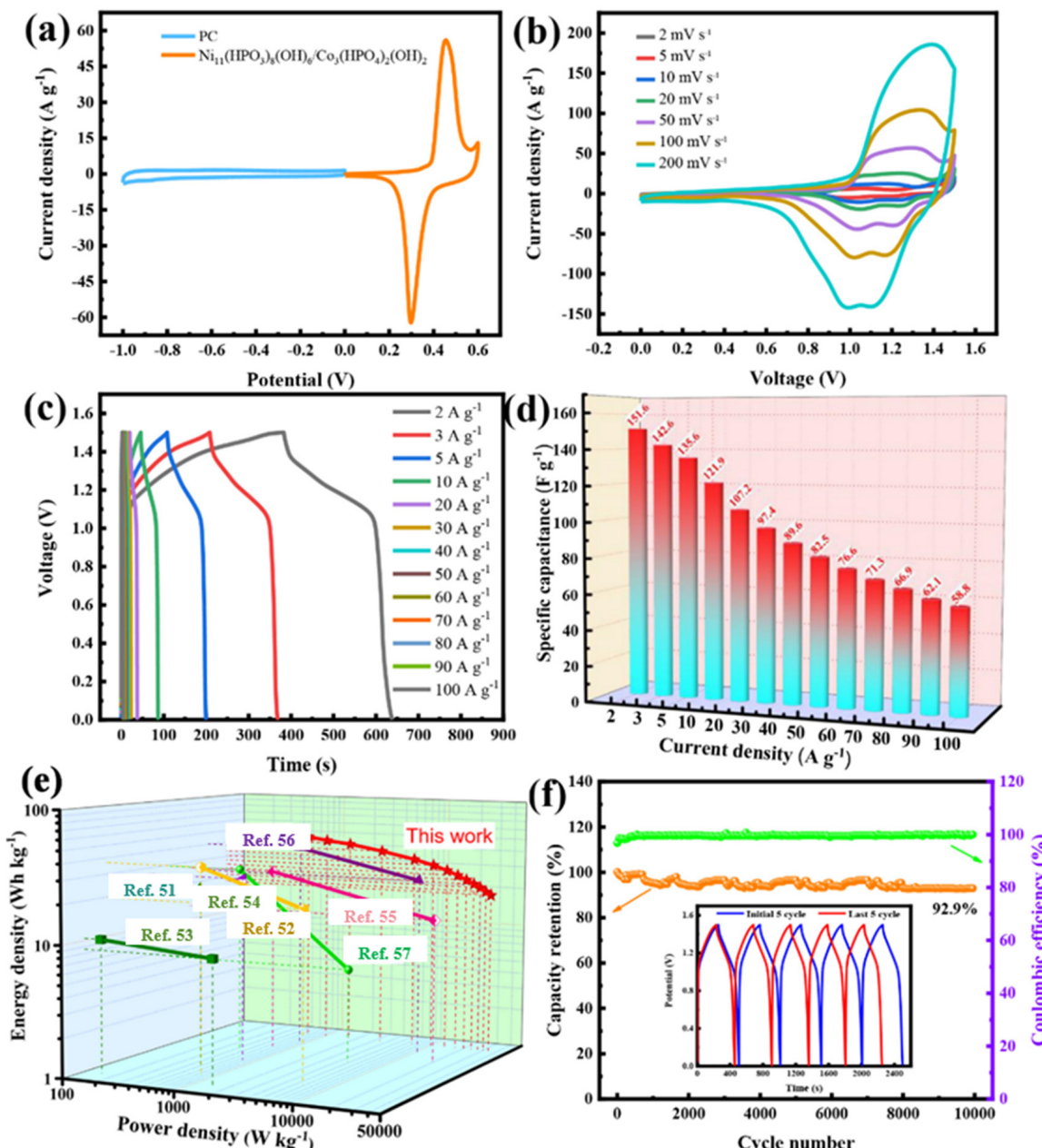


Figure 6. Electrochemical performance of $\text{Ni}_{11}(\text{HPO}_3)_8(\text{OH})_6/\text{Co}_3(\text{HPO}_4)_2(\text{OH})_2$ // PC HSC: (a) CV profiles of PC and $\text{Ni}_{11}(\text{HPO}_3)_8(\text{OH})_6/\text{Co}_3(\text{HPO}_4)_2(\text{OH})_2$ electrodes at 10 mV s^{-1} . (b) CV profiles, (c) GCD profiles, (d) rate performance diagram, (e) Ragone plot, and (f) circulation characteristics and the Coulombic efficiency at 3 A g^{-1} after 10,000 cycles, inset picture shows the pre/post five GCD curves.

4. Conclusions

In summary, the $\text{Ni}_{11}(\text{HPO}_3)_8(\text{OH})_6/\text{Co}_3(\text{HPO}_4)_2(\text{OH})_2$ heterostructured material consisting of flakes has been synthesized through one-step hydrothermal process. Benefiting from its intricate multi-scale porosity architecture and the synergistic effect, the prepared $\text{Ni}_{11}(\text{HPO}_3)_8(\text{OH})_6/\text{Co}_3(\text{HPO}_4)_2(\text{OH})_2$ composite electrode demonstrates excellent cycling endurance and rate capability in alkaline conditions. Specifically, the $\text{Ni}_{11}(\text{HPO}_3)_8(\text{OH})_6/\text{Co}_3(\text{HPO}_4)_2(\text{OH})_2$ composite electrode exhibits superior capacity retention capabilities, with 82.5% retention at 50 A g^{-1} and 71% even at the elevated currently densities of 100 A g^{-1} . Moreover, it sustains an impressive 92.7% capacity retention after enduring 5000 cycles at 10 A g^{-1} . In addition, the $\text{Ni}_{11}(\text{HPO}_3)_8(\text{OH})_6/\text{Co}_3(\text{HPO}_4)_2(\text{OH})_2$ // PC

HSC device showcases exceptional performance, featuring a heightened energy density of 47.4 Wh kg^{-1} alongside a superlative power density of 36 kW kg^{-1} . Notably, after enduring 10,000 cycles, it retains a good 92.9% capacity at 3 A g^{-1} . Obtained from the above data, the $\text{Ni}_{11}(\text{HPO}_3)_8(\text{OH})_6/\text{Co}_3(\text{HPO}_4)_2(\text{OH})_2$ heterostructured materials are likely candidates for electrode materials for high-performance HSC. Additionally, this hydrothermal synthesis method, with its low cost and simple process, provides a feasible idea for constructing phosphate heterostructured materials with excellent properties that may be applied to future storage systems.

Author Contributions: Writing—original draft preparation, K.L.; writing—review and editing, M.J., Y.Z. (Yirong Zhu) and C.L.; project administration, M.J. and Y.Z. (Yirong Zhu); formal analysis T.W. and Y.Z. (Yang Zhang); investigation, R.L. and X.W.; resources, L.L. and S.Z.; data curation, K.L. and Y.Z (Yang Zhang). All authors have read and agreed to the published version of the manuscript.

Funding: This research was funded by the Distinguished Young Scholar Fund Project of Hunan Province Natural Science Foundation (No. 2023JJ10041), the Hunan Provincial Education Office Foundation of China (No. 22A0114), the Natural Science Foundation of Henan Province (232300421228), the Topnotch Talents Program of Henan Agricultural University (30501032), and the National Natural Science Foundation of China (22305070).

Data Availability Statement: The dataset is available on request from the authors.

Conflicts of Interest: The authors declare no conflicts of interest.

References

- Pomerantseva, E.; Bonaccorso, F.; Feng, X.; Cui, Y.; Gogotsi, Y. Energy storage: The future enabled by nanomaterials. *Science* **2019**, *366*, eaan8285. [[CrossRef](#)] [[PubMed](#)]
- Bi, S.; Banda, H.; Chen, M.; Niu, L.; Chen, M.; Wu, T.; Wang, J.; Wang, R.; Feng, J.; Chen, T.; et al. Molecular understanding of charge storage and charging dynamics in supercapacitors with MOF electrodes and ionic liquid electrolytes. *Nat. Mater.* **2020**, *19*, 552–558. [[CrossRef](#)] [[PubMed](#)]
- Zhang, Q.-Z.; Zhang, D.; Miao, Z.-C.; Zhang, X.-L.; Chou, S.-L. Research Progress in MnO_2 –Carbon Based Supercapacitor Electrode Materials. *Small* **2018**, *14*, 1702883. [[CrossRef](#)] [[PubMed](#)]
- Lee, J.-H.; Yang, G.; Kim, C.-H.; Mahajan, R.L.; Lee, S.-Y.; Park, S.-J. Flexible solid-state hybrid supercapacitors for the internet of everything (IoE). *Energy Environ. Sci.* **2022**, *15*, 2233–2258. [[CrossRef](#)]
- Zhao, Z.; Ye, Y.; Zhu, W.; Xiao, L.; Deng, B.; Liu, J. Bismuth oxide nanoflake@carbon film: A free-standing battery-type electrode for aqueous sodium ion hybrid supercapacitors. *Chin. Chem. Lett.* **2018**, *29*, 629–632. [[CrossRef](#)]
- Amiri, A.; Bruno, A.; Polycarpou, A.A. Configuration-dependent stretchable all-solid-state supercapacitors and hybrid supercapacitors. *Carbon Energy* **2023**, *5*, e320. [[CrossRef](#)]
- Sadavar, S.; Wang, K.J.; Kang, T.; Hwang, M.; Saeed, G.; Yu, X.; Park, H.S. Anion storage for hybrid supercapacitor. *Mater. Today Energy* **2023**, *37*, 101388. [[CrossRef](#)]
- Wang, X.; Yan, C.; Yan, J.; Sumboja, A.; Lee, P.S. Orthorhombic niobium oxide nanowires for next generation hybrid supercapacitor device. *Nano Energy* **2015**, *11*, 765–772. [[CrossRef](#)]
- Sun, L.; Liu, Y.; Yan, M.; Yang, Q.; Liu, X.; Shi, W. Lewis acid etched $\text{Ni}_x\text{Co}_{1-x}\text{Se}_2$ derived from ZIF-L on CoO nanowires for hybrid-supercapacitors. *Chem. Eng. J.* **2022**, *431*, 133472. [[CrossRef](#)]
- Roy, A.; Inta, H.R.; Ghosh, S.; Koppisetti, H.V.S.R.M.; Mondal, A.; Verma, B.R.; Bag, S.; Mahalingam, V. Electrochemical surface reconstruction of nickel cobalt pyrophosphate to Ni/Co-hydroxide-(oxy)hydroxide: An efficient and highly durable battery-type supercapacitor electrode material. *J. Mater. Chem. A* **2024**, *12*, 4086–4098. [[CrossRef](#)]
- Salunkhe, R.R.; Kaneti, Y.V.; Yamauchi, Y. Metal–Organic Framework-Derived Nanoporous Metal Oxides toward Supercapacitor Applications: Progress and Prospects. *ACS Nano* **2017**, *11*, 5293–5308. [[CrossRef](#)] [[PubMed](#)]
- Yu, X.Y.; Lou, X.W. Mixed Metal Sulfides for Electrochemical Energy Storage and Conversion. *Adv. Funct. Mater.* **2018**, *8*, 1701592. [[CrossRef](#)]
- Zou, K.; Deng, W.; Silvester, D.S.; Zou, G.; Hou, H.; Banks, C.E.; Li, L.; Hu, J.; Ji, X. Carbonyl Chemistry for Advanced Electrochemical Energy Storage Systems. *ACS Nano* **2024**, *18*, 19950–20000. [[CrossRef](#)] [[PubMed](#)]
- Zan, G.; Li, S.; Chen, P.; Dong, K.; Wu, Q.; Wu, T. Mesoporous Cubic Nanocages Assembled by Coupled Monolayers With 100% Theoretical Capacity and Robust Cycling. *ACS Cent. Sci.* **2024**, *10*, 1283–1294. [[CrossRef](#)]
- Manikandan, R.; Savariraj, A.D.; Nagaraju, G.; Kale, A.M.; Puigdollers, J.; Park, H.; Kim, H.-S.; Oh, J.-M.; Raj, C.J.; Kim, B.C. Mixed-phase composites derived from cobalt terephthalate as efficient battery-type electrodes for high-performance supercapattery. *J. Mater. Sci. Technol.* **2023**, *157*, 220–233. [[CrossRef](#)]

16. Manikandan, R.; Raj, C.J.; Goli, N.; Oh, J.-M.; Kim, B.C.; Periyasamy, S.; Lee, J. Interconnected Vanadyl Pyrophosphate Nanonetworks as a Flexible Electrode for High-Voltage and Long-Life Li-Ion Supercapacitors. *Appl. Mater. Interfaces* **2023**, *15*, 25452–25461. [[CrossRef](#)]
17. Zhao, H.; Yuan, Z.-Y. Design Strategies of Transition-Metal Phosphate and Phosphonate Electrocatalysts for Energy-Related Reactions. *Chem. Eng. Sci.* **2021**, *14*, 130–149. [[CrossRef](#)]
18. Cheng, Q.; Zhao, X.; Yang, G.; Mao, L.; Liao, F.; Chen, L.; He, P.; Pan, D.; Chen, S. Recent advances of metal phosphates-based electrodes for high-performance metal ion batteries. *Energy Storage Mater.* **2021**, *41*, 842–882. [[CrossRef](#)]
19. Wang, D.; Wang, Y.; Fu, Z.; Xu, Y.; Yang, L.-X.; Wang, F.; Guo, X.; Sun, W.; Yang, Z.-L. Cobalt–Nickel Phosphate Composites for the All-Phosphate Asymmetric Supercapacitor and Oxygen Evolution Reaction. *Appl. Mater. Interfaces* **2021**, *13*, 34507–34517. [[CrossRef](#)]
20. Xie, L.; Zong, Q.; Zhang, Q.; Sun, J.; Zhou, Z.; He, B.; Zhu, Z.; E, S.; Yao, Y. Hierarchical NiCoP nanosheet arrays with enhanced electrochemical properties for high-performance wearable hybrid capacitors. *J. Alloys Compd.* **2019**, *781*, 783–789. [[CrossRef](#)]
21. Fan, J.; Wu, K.; Chen, A.; Wang, M.; Xie, X.; Fan, J. Fingerprint-like NiCoP electrode material with rapid charging/discharging performance under large current density. *J. Alloys Compd.* **2022**, *902*, 163866. [[CrossRef](#)]
22. Liu, M.; Li, J.; Han, W.; Kang, L. Simple synthesis of novel phosphate electrode materials with unique microstructure and enhanced supercapacitive properties. *J. Energy Chem.* **2016**, *25*, 601–608. [[CrossRef](#)]
23. Zhang, Y.; Zheng, M.; Qu, M.; Sun, M.; Pang, H. Core–shell $\text{Co}_{11}(\text{HPO}_3)_8(\text{OH})_6\text{-Co}_3\text{O}_4$ hybrids for high-performance flexible all-solid-state asymmetric supercapacitors. *J. Alloys Compd.* **2015**, *651*, 214–221. [[CrossRef](#)]
24. Li, X.; Elshahawy, A.M.; Guan, C.; Wang, J. Metal Phosphides and Phosphates-based Electrodes for Electrochemical Supercapacitors. *Small* **2017**, *13*, 1701530. [[CrossRef](#)] [[PubMed](#)]
25. Wang, X.; Zhai, X.; Lv, P.; Jiao, Y.; Wang, S.; Chi, J. Amorphous nickel phosphate as a high performance electrode material for supercapacitor. *Synth. Met.* **2023**, *292*, 117217. [[CrossRef](#)]
26. Zhang, Y.-N.; Su, C.-Y.; Chen, J.-L.; Huang, W.-H.; Lou, R. Recent progress of transition metal-based biomass-derived carbon composites for supercapacitor. *Rare Met.* **2023**, *42*, 769–796. [[CrossRef](#)]
27. Zhang, G.C.; Feng, M.; Li, Q.; Wang, Z.; Fang, Z.; Niu, Z.; Qu, N.; Fan, X.; Li, S.; Gu, J.; et al. High Energy Density in Combination with High Cycling Stability in Hybrid Supercapacitors. *Appl. Mater. Interfaces* **2022**, *14*, 2674–2682. [[CrossRef](#)]
28. Mirghni, A.A.; Madito, M.J.; Oyedotun, K.O.; Masikhwa, T.M.; Ndiaye, N.M.; Ray, S.J.; Manyala, N. A high energy density asymmetric supercapacitor utilizing a nickel phosphate/graphene foam composite as the cathode and carbonized iron cations adsorbed onto polyaniline as the anode. *RSC Adv.* **2018**, *8*, 11608–11621. [[CrossRef](#)]
29. Chen, G.; Yan, L.; Luo, H.; Guo, S. Nanoscale Engineering of Heterostructured Anode Materials for Boosting Lithium-Ion Storage. *Adv. Mater.* **2016**, *28*, 7580–7602. [[CrossRef](#)]
30. Lin, Y.; Sun, K.; Liu, S.; Chen, X.; Cheng, Y.; Cheong, W.-C.; Chen, Z.; Zheng, L.; Zhang, J.; Li, X.; et al. Construction of CoP/NiCoP Nanotadpoles Heterojunction Interface for Wide pH Hydrogen Evolution Electrocatalysis and Supercapacitor. *Adv. Funct. Mater.* **2019**, *9*, 1901213. [[CrossRef](#)]
31. Liu, X.; Zhu, Y.; Lu, Z.; Xiao, J.; Zou, G.; Hou, H.; Ji, X. Heterostructured flower-like $\text{NiO}/\text{Co}_3\text{O}_4$ microspheres modified by bifunctional carbon quantum dots as a battery-type cathode for high energy and power density hybrid supercapacitors. *Carbon Neutralization* **2023**, *2*, 721–737. [[CrossRef](#)]
32. Li, Y.; Zhang, J.; Chen, Q.; Xia, X.; Chen, M. Emerging of Heterostructure Materials in Energy Storage: A Review. *Adv. Mater.* **2021**, *33*, 2100855. [[CrossRef](#)] [[PubMed](#)]
33. Yun, X.; Lu, T.; Zhou, R.; Lu, Z.; Li, J.; Zhu, Y. Heterostructured $\text{NiSe}_2/\text{CoSe}_2$ hollow microspheres as battery-type cathode for hybrid supercapacitors: Electrochemical kinetics and energy storage mechanism. *Chem. Eng. J.* **2021**, *426*, 131328. [[CrossRef](#)]
34. Li, M.; Li, M.; Zhao, M.; Wu, B.; Mourdikoudis, S.; Wei, S.; Oliveira, F.M.; He, J.; Děkanovský, L.; Luxa, J.; et al. Rational design of crystalline/amorphous nickel manganese phosphate octahydrate heterostructure for high-performance aqueous and all-solid-state asymmetric supercapacitors. *Chem. Eng. J.* **2024**, *482*, 148895. [[CrossRef](#)]
35. Jiang, T.; Zhang, Y.; Du, C.; Xiao, T.; Wan, L. Two-step electrodeposition synthesis of iron cobalt selenide and nickel cobalt phosphate heterostructure for hybrid supercapacitors. *J. Colloid Interface Sci.* **2023**, *629*, 1049–1060. [[CrossRef](#)]
36. Davidson, A.; Tempere, J.F.; Che, M.; Roulet, H.; Dufour, G. Spectroscopic Studies of Nickel(II) and Nickel(III) Species Generated upon Thermal Treatments of Nickel/Ceria-Supported Materials. *J. Phys. Chem.* **1996**, *100*, 4919–4929. [[CrossRef](#)]
37. Casella, I.G.; Gatta, M. Electrochemical and XPS Characterization of Composite Modified Electrodes Obtained by Nickel Deposition on Noble Metals. *Anal. Chem.* **2000**, *72*, 2969–2975. [[CrossRef](#)]
38. Huang, J.; Xiong, Y.; Peng, Z.; Chen, L.; Wang, L.; Xu, Y.; Tan, L.; Yuan, K.; Chen, Y. A General Electrodeposition Strategy for Fabricating Ultrathin Nickel Cobalt Phosphate Nanosheets with Ultrahigh Capacity and Rate Performance. *ACS Nano* **2020**, *14*, 14201–14211. [[CrossRef](#)]
39. Dan, H.; Tao, K.; Zhou, Q.; Gong, Y.; Lin, J. Ni-Doped Cobalt Phosphite, $\text{Co}_{11}(\text{HPO}_3)_8(\text{OH})_6$, with Different Morphologies Grown on Ni Foam Hydro(sollo)thermally for High-Performance Supercapacitor. *Appl. Mater. Interfaces* **2018**, *10*, 31340–31354. [[CrossRef](#)]
40. Li, X.; Wu, H.; Elshahawy, A.M.; Wang, L.; Pennycook, S.J.; Guan, C.; Wang, J. Cactus-Like NiCoP/NiCo-OH 3D Architecture with Tunable Composition for High-Performance Electrochemical Capacitors. *Adv. Funct. Mater.* **2018**, *28*, 1800036. [[CrossRef](#)]

41. Ding, R.; Li, X.; Shi, W.; Xu, Q.; Liu, E. One-pot solvothermal synthesis of ternary Ni-Co-P micro/nano-structured materials for high performance aqueous asymmetric supercapacitors. *Chem. Eng. J.* **2017**, *320*, 376–388. [[CrossRef](#)]
42. Hu, Y.-M.; Liu, M.-C.; Hu, Y.-X.; Yang, Q.-Q.; Kong, L.-B.; Kang, L. One-pot hydrothermal synthesis of porous nickel cobalt phosphides with high conductivity for advanced energy conversion and storage. *Electrochim. Acta* **2016**, *215*, 114–125. [[CrossRef](#)]
43. Li, B.; Gu, P.; Feng, Y.; Zhang, G.; Huang, K.; Xue, H.; Pang, H. Ultrathin Nickel–Cobalt Phosphate 2D Nanosheets for Electrochemical Energy Storage under Aqueous/Solid-State Electrolyte. *Adv. Funct. Mater.* **2017**, *27*, 1605784. [[CrossRef](#)]
44. Liang, B.; Chen, Y.; He, J.; Chen, C.; Liu, W.; He, Y.; Liu, X.; Zhang, N.; Roy, V.A.L. Controllable Fabrication and Tuned Electrochemical Performance of Potassium Co–Ni Phosphate Microplates as Electrodes in Supercapacitors. *Appl. Mater. Interfaces* **2018**, *10*, 3506–3514. [[CrossRef](#)]
45. Zhang, J.; Yang, Y.; Zhang, Z.; Xu, X.; Wang, X. Rapid synthesis of mesoporous $\text{Ni}_x\text{Co}_{3-x}(\text{PO}_4)_2$ hollow shells showing enhanced electrocatalytic and supercapacitor performance. *J. Mater. Chem. A* **2014**, *2*, 20182–20188. [[CrossRef](#)]
46. Chen, C.; Zhang, N.; He, Y.; Liang, B.; Ma, R.; Liu, X. Controllable Fabrication of Amorphous Co–Ni Pyrophosphates for Tuning Electrochemical Performance in Supercapacitors. *Appl. Mater. Interfaces* **2016**, *8*, 23114–23121. [[CrossRef](#)]
47. Li, B.; Shi, Y.; Huang, K.; Zhao, M.; Qiu, J.; Xue, H.; Pang, H. Cobalt-Doped Nickel Phosphite for High Performance of Electrochemical Energy Storage. *Small* **2018**, *14*, 1703811. [[CrossRef](#)]
48. Zhao, Y.; Chen, Z.; Xiong, D.-B.; Qiao, Y.; Tang, Y.; Gao, F. Hybridized Phosphate with Ultrathin Nanoslices and Single Crystal Microplatelets for High Performance Supercapacitors. *Sci. Rep.* **2016**, *6*, 17613. [[CrossRef](#)]
49. Tang, Y.; Liu, Z.; Guo, W.; Chen, T.; Qiao, Y.; Mu, S.; Zhao, Y.; Gao, F. Honeycomb-like mesoporous cobalt nickel phosphate nanospheres as novel materials for high performance supercapacitor. *Electrochim. Acta* **2016**, *190*, 118–125. [[CrossRef](#)]
50. Elshahawy, A.M.; Guan, C.; Li, X.; Zhang, H.; Hu, Y.; Wu, H.; Pennycook, S.J.; Wang, J. Sulfur-doped cobalt phosphide nanotube arrays for highly stable hybrid supercapacitor. *Nano Energy* **2017**, *39*, 162–171. [[CrossRef](#)]
51. Mao, H.; Zhang, F.; Liu, X.; Qiu, J.; Li, B.; Jin, Z. Synthesis of cobalt phosphate nanoflakes for high-performance flexible symmetric supercapacitors. *J. Mater. Sci. Mater. Electron.* **2018**, *29*, 16721–16729. [[CrossRef](#)]
52. Pang, H.; Wang, S.; Shao, W.; Zhao, S.; Yan, B.; Li, X.; Li, S.; Chen, J.; Du, W. Few-layered $\text{CoHPO}_4 \cdot 3\text{H}_2\text{O}$ ultrathin nanosheets for high performance of electrode materials for supercapacitors. *Nanoscale* **2013**, *5*, 5752–5757. [[CrossRef](#)] [[PubMed](#)]
53. Pang, H.; Yan, Z.; Wang, W.; Chen, J.; Zhang, J.; Zheng, H. Facile fabrication of $\text{NH}_4\text{CoPO}_4 \cdot \text{H}_2\text{O}$ nano/microstructures and their primarily application as electrochemical supercapacitor. *Nanoscale* **2012**, *4*, 5946–5953. [[CrossRef](#)] [[PubMed](#)]
54. Lan, Y.; Zhao, H.; Zong, Y.; Li, X.; Sun, Y.; Feng, J.; Wang, Y.; Zheng, X.; Du, Y. Phosphorization boosts the capacitance of mixed metal nanosheet arrays for high performance supercapacitor electrodes. *Nanoscale* **2018**, *10*, 11775–11781. [[CrossRef](#)] [[PubMed](#)]
55. Chen, H.C.; Jiang, S.; Xu, B.; Huang, C.; Hu, Y.; Qin, Y.; He, M.; Cao, H. Sea-urchin-like nickel–cobalt phosphide/phosphate composites as advanced battery materials for hybrid supercapacitors. *J. Mater. Chem. A* **2019**, *7*, 6241–6249. [[CrossRef](#)]
56. Ning, W.-W.; Chen, L.-B.; Wei, W.-F.; Chen, Y.-J.; Zhang, X.-Y. $\text{NiCoO}_2/\text{NiCoP@Ni}$ nanowire arrays: Tunable composition and unique structure design for high-performance winding asymmetric hybrid supercapacitors. *Rare Met.* **2020**, *39*, 1034–1044. [[CrossRef](#)]
57. Li, H.; Yu, H.; Zhai, J.; Sun, L.; Yang, H.; Xie, S. Self-assembled 3D cobalt phosphate octahydrate architecture for supercapacitor electrodes. *Mater. Lett.* **2015**, *152*, 25–28. [[CrossRef](#)]

Disclaimer/Publisher’s Note: The statements, opinions and data contained in all publications are solely those of the individual author(s) and contributor(s) and not of MDPI and/or the editor(s). MDPI and/or the editor(s) disclaim responsibility for any injury to people or property resulting from any ideas, methods, instructions or products referred to in the content.